A numerical model for aerated-water wave breaking

L.-R. Plumerault [1], D. Astruc [2,*,†], P. Villedieu [3] and P. Maron [1]

[1] *SIAME-IVS, Allée du Parc Montaury, 64600, Anglet, France*
[2] *Université de Toulouse; INPT, UPS; IMFT, Allée Camille Soula, F-31400 Toulouse, France. CNRS; IMFT; F-31400 Toulouse, France*
[3] *ONERA Centre de Toulouse - 2av. Edouard Belin, BP 4025-31055, Toulouse Cedex 4, France*

SUMMARY

This work presents a numerical model designed for the simulation of water-wave impacts on a structure when aeration of the liquid phase is considered. The model is based on a multifluid Navier–Stokes approach in which all fluids are assumed compressible. The numerical method is based on a finite volume algorithm in space and a second order Runge–Kutta method in time. A validation of this model is performed. It shows a good accuracy for acoustic and shock wave propagation in a bubbly liquid and for wave breaking. Copyright

KEY WORDS: numerical model; Navier–Stokes; wave breaking; compressible

1. INTRODUCTION

The numerical simulation of wave impacts on coastal structures represents a challenging problem for the modeller as it encompasses a wide range of physical processes. One of the main issues for wave impacts is to estimate their mechanical strength. Thus, an accurate modelling of the pressure field is necessary. The pressure dynamics is controlled by several physical mechanisms. Particularly, a wave-impact flow includes some entrained air as bubbles in the water and the entrapment of an air pocket that can present a complex behaviour, see for instance [1–3]. The simulation of wave impacts has been tackled with different models and methods. Although there were attempts to use other approaches, recently, the most widespread model used to represent wave breaking or wave impacts is the Navier–Stokes model. A few authors tried to validate incompressible one-fluid models for wave impact computations [4, 5] using a volume of fluid approach. However the incompressible flow approximation did not allow for a precise description of the dynamics of the pressure field induced by impact. Indeed, as wave impacts occur in a mixture of air and water, it is important to distinguish the air entrapped as an air pocket by the overturning wave and the air entrained as bubbles by the flow. The simulation of wave impacts thus requires to take into account the compressibility of the flow because of the presence of air either as pockets or as bubbles [6]. In the present work, we propose a fully compressible approach on the basis of a multifluid model. [7] developed a two-phase compressible flow model, which was used as a basis for the model presented in this paper. It was based on a compressible multifluid model and a relaxation method [8]. Although it was appropriate for the simulation of two-phase flows in the limit of separated-phase flows, it was not suitable for cases of dispersed-phase flows. Figure 1 shows the air and water sound speed and the physical mixture sound speed from [9].

*Correspondence to: D. Astruc, Institut de Mécanique des Fluides de Toulouse, Allée du Pr. C. Soula, 31400 Toulouse France.
†E-mail: astruc@imft.fr

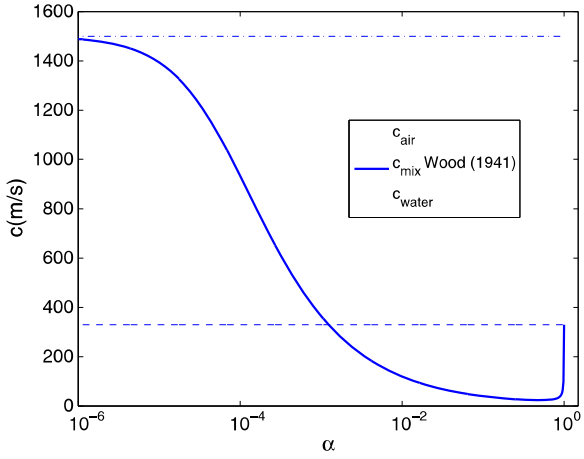

Figure 1. Air-water mixture sound speed.

The sound speed in Chanteperdrix's model [7] is only representative of the physical one when volume fraction is close to 0 or 1, that is, for separated-phase flows only. Therefore, a more detailed model was required to properly estimate pressure fields in dispersed-phase flows such as bubbly water.

As wave impact is a problem that includes both the separated-phase limit (presence of the free surface and air pockets) and the dispersed-phase limit (presence of bubbles within water), we chose for the new model to be able to distinguish the gas phase included in the liquid phase from the gas above the free surface. Indeed this feature will allow to set a particular behaviour to the gas phase trapped in water such as subgrid scale models for the rise of bubbles. This is a prospective approach and it has not been implemented in the present work yet.

There is an intrinsic difference of scale between the air pockets and the bubbles. In the new model, the air pockets are explicitly described, allowing for the description of their oscillations. The bubbles though are not spatially resolved and are going to interact with the flow by modifying the properties of the liquid phase in terms of density and sound speed.

Section 2 presents the mathematical model, which can be seen as an improvement of Chanteperdrix's model [7]. Section 3 deals with the numerical implementation. Sections 4.1 to 4.3 present the different validation tests. Finally, concluding remarks are proposed.

2. THREE-FLUID MODEL

Let us consider a free-surface flow of three viscous fluids: the air above the free surface, the water and the air within the water. We model this physical situation by a general mixture composed of fluids 1 and 2 composed of fluids w and a. Fluid 1 represents the air above the free surface. Fluid 2 is the mixture of air below the free surface that we call fluid 'a' and water that we call fluid 'w'. So, the enhancement of Chanteperdrix's model [7] is to consider that fluid 2 itself is a mixture. Let us note that this configuration allows for fluids 1 and 2 to flow as separate phases and for fluids 'a' and 'w' to flow as dispersed phases.

For the derivation of the mathematical model, we assume that we are at the macroscopic scale defined by [10], thus the control volume V_{tot} over which the average process is undertaken is larger than the typical size of the air bubbles. We assume no phase change and isothermal flow. Moreover, both fluids are supposed barotropic. $\alpha = \frac{V_1}{V_{\text{tot}}}$ is the volume fraction of fluid 1 in a control volume containing a mixture of fluids 1 and 2. Let us introduce $\beta = \frac{V_a}{V_2}$, the volume fraction of fluid a within fluid 2. And let $y = \frac{m_a}{m_2}$, be the mass fraction of fluid a within fluid 2 (see Figure 2).

We assume no slip between fluids so that they all move at the same velocity $\underline{V}$. We note ρ_1, ρ_2, ρ_a, and ρ_w, the respective density of each fluid.

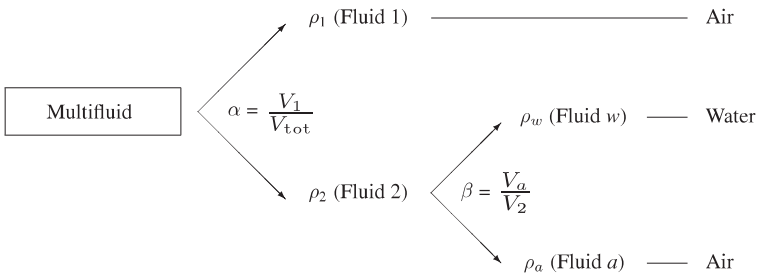

Figure 2. Scheme of the three-fluid model principle.

For sake of clarity, we introduce the following notations:

$$\begin{aligned}\tilde{\rho}_1 &= \alpha\rho_1\\ \tilde{\rho}_2 &= (1-\alpha)\rho_2\\ \tilde{\rho}_a &= \beta\rho_a\\ \tilde{\rho}_w &= (1-\beta)\rho_w\end{aligned} \tag{1}$$

From these definitions, we obtain the following:

$$\tilde{\rho}_a = \beta\rho_a = y\rho_2 = y\frac{\tilde{\rho}_2}{1-\alpha} \tag{2}$$

$$\tilde{\rho}_w = (1-\beta)\rho_w = (1-y)\rho_2 = (1-y)\frac{\tilde{\rho}_2}{1-\alpha} \tag{3}$$

2.1. Conservation equations

As the idea of this model is to deal with three fluids (fluids 1, a and w), it requires three mass conservation equations. We assume no slip between fluids, thus the velocity field is unique. It is denoted as $\underline{V}$. First, we use a mass conservation equation for each of fluids 1 and 2:

$$\frac{\partial\tilde{\rho}_i}{\partial t} + \nabla.(\tilde{\rho}_i\underline{V}) \quad = 0 \quad \text{with } i = 1,2$$

Then, the transport of mass of fluid a (air within fluid 2) regarding the general mixture $\frac{m_a}{V_{\text{tot}}} = \tilde{\rho}_2 y$ (using definitions) is governed by the following:

$$\frac{\partial y}{\partial t} + \underline{V}.\nabla(y) \quad = 0 \tag{4}$$

Equation (4) can be written in conservative form by multiplying it by $\tilde{\rho}_2$ and adding the product of y and the mass conservation equation for fluid 2 (Equation (6)). This leads to a conservation equation for the mass of fluid a:

$$\frac{\partial(\tilde{\rho}_2 y)}{\partial t} + \nabla.(\tilde{\rho}_2 y\,\underline{V}) \quad = 0$$

Therefore, the conservative variables are $\tilde{\rho}_1$, $\tilde{\rho}_2$, $\tilde{\rho}_2 y$ and $\rho\underline{V}$, where $\rho = \alpha\rho_1 + (1-\alpha)\rho_2$. We denote P as the pressure in the mixture, μ the mixture viscosity, τ^D the mixture viscous stress tensor and $\underline{F}$ the external forces. Given the space scales associated with wave impact, the capillary

forces are neglected here; however, they could be accounted for in such a model [11]. The governing conservation equations of the model thus read as follows:

$$\frac{\partial \tilde{\rho}_1}{\partial t} + \nabla.(\tilde{\rho}_1 \underline{V}) = 0 \tag{5}$$

$$\frac{\partial \tilde{\rho}_2}{\partial t} + \nabla.(\tilde{\rho}_2 \underline{V}) = 0 \tag{6}$$

$$\frac{\partial (\tilde{\rho}_2 y)}{\partial t} + \nabla.(\tilde{\rho}_2 y\, \underline{V}) = 0 \tag{7}$$

$$\frac{\partial \rho \underline{V}}{\partial t} + \nabla.\left(\rho \underline{V} \otimes \underline{V} + P(\tilde{\rho}_1, \tilde{\rho}_2, \tilde{\rho}_2 y)\, \underline{I}\right) = \nabla.\tau^D + \underline{F} \tag{8}$$

We note P_i as the pressure in fluid i, and μ_i the viscosity of fluid i.

The mixture law for density reads as follows:

$$\rho = \alpha\rho_1 + (1-\alpha)\rho_2 \tag{9}$$

with

$$\rho_2 = \beta\rho_a + (1-\beta)\rho_w \tag{10}$$

The mixture law for viscosity reads as follows:

$$\mu = \alpha\mu_1 + (1-\alpha)\mu_2 \tag{11}$$

with

$$\mu_2 = \beta\mu_a + (1-\beta)\mu_w \tag{12}$$

The mixture law for pressure reads as follows:

$$P = \alpha P_1 + (1-\alpha) P_2 \tag{13}$$

with

$$P_2 = \beta P_a + (1-\beta) P_w \tag{14}$$

Finally, one obtains eight unknowns $\tilde{\rho}_1$, $\tilde{\rho}_2$, $\tilde{\rho}_2 y$, $\rho\underline{V}$, α, β, and six Equations (5–8). Two more equations must be introduced to close the model.

2.2. Pressure equilibria

Chanteperdrix's model [7] was closed by assuming pressure equilibrium between fluids 1 and 2:

$$P_1 = P_2 \tag{15}$$

which allowed for the computation of the volume fraction α and the mixture pressure P. This equation remains the same here. In the three-fluid model, the mass conservation of fluid a is ensured by Equation (5). However, another variable is introduced, the mass (or volume) fraction of fluid a: y (or β). Thus, one more equation is required to close the model. For the sake of coherence, we set the following:

$$P_a = P_w \tag{16}$$

This means that, in this model, the relaxation process regarding pressures is assumed to be instantaneous. In the same way, the assumption of no-slip between fluids can be regarded as the velocity relaxation being instantaneous.

2.3. Equations of state

In this section, we introduce the equations of state corresponding to each fluid. One can notice that we use the terminology 'equations of state' by abuse because it would imply equations that describe all states that each fluid can undertake independently from the transformation path. And thus, it would involve the internal energy of each phase. However, as long as we do not consider the energy conservation equation for the motion of the phases, we implicitly assume that, for all transformations, the internal energy is constant. We are therefore conscious that the rigorous expression is 'transformation equation'.

2.3.1. Equation of state for fluid 1. Equation of state for fluid 1 is taken to be linear around a reference state P_{1_0}, which will be, in this study, the atmospheric pressure. It reads as follows:

$$P_1(\rho_1) = P_{1_0} + c_{1_0}^2(\rho_1 - \rho_{1_0}) \tag{17}$$

c_{1_0} is the sound speed in fluid 1 at P_{1_0} and ρ_{1_0} is the density of fluid 1 at P_{1_0}. Equation (17) can be rewritten upon conservative variables $\tilde{\rho}_1$ and α using (1):

$$P_1(\tilde{\rho}_1, \alpha) = P_{1_0} + c_{1_0}^2\left(\frac{\tilde{\rho}_1}{\alpha} - \rho_{1_0}\right) \tag{18}$$

2.3.2. Equation of state for fluid a. Fluid-a (pure air) pressure is chosen to behave according to a polytropic law:

$$P_a(\rho_a) = \frac{P_{a_0}}{\rho_{a_0}^k}\rho_a^k \tag{19}$$

where ρ_{a_0} is the density of fluid a at reference pressure P_{a_0}, which will be, in this study, the atmospheric pressure. Equation (19) can be rewritten upon conservative variable $y\tilde{\rho}_2$ and α and β using relation (2):

$$P_a(y\tilde{\rho}_2, \alpha, \beta) = \frac{P_{a_0}}{\rho_{a_0}^k}\left(\frac{y\tilde{\rho}_2}{\beta(1-\alpha)}\right)^k \tag{20}$$

2.3.3. Equation of state for fluid w. Fluid-w (pure water) pressure is chosen to behave linearly upon density around a constant reference state (P_{w_0}, ρ_{w_0}), which will be, in this study, the atmospheric pressure. It reads as follows:

$$P_w(\rho_w) = P_{w_0} + c_{w_0}^2(\rho_w - \rho_{w_0}) \tag{21}$$

where c_{w_0} is the sound speed in pure water at P_{w_0}. Equation (21) can be rewritten upon conservative variables $\tilde{\rho}_2$ and $y\tilde{\rho}_2$ and α and β using relation (3):

$$P_w(\tilde{\rho}_2, y\tilde{\rho}_2, \alpha, \beta) = P_{w_0} + c_{w_0}^2\left(\frac{(1-y)\tilde{\rho}_2}{(1-\beta)(1-\alpha)} - \rho_{w_0}\right) \tag{22}$$

2.3.4. Equation of state of fluid 2. Equation of state of fluid 2 is obtained from the combination of equations of state of fluids a (19) and w (21) within fluid 2 and pressure closure Equation (14):

$$P_2(\rho_a, \rho_w, \beta) = \beta\frac{P_{a_0}}{\rho_{a_0}^k}(\rho_a)^k + (1-\beta)\left[P_{w_0} + c_{w_0}^2(\rho_w - \rho_{w_0})\right] \tag{23}$$

It is useful for further developments to rewrite Equation (23) upon conservative variables $\tilde{\rho}_2$ and $y\tilde{\rho}_2$ and α and β using relations (2) and (3), this form reads as follows:

$$P_2(\tilde{\rho}_2, y\tilde{\rho}_2, \alpha, \beta) = \beta\frac{P_{a_0}}{\rho_{a_0}^k}\left(\frac{y\tilde{\rho}_2}{\beta(1-\alpha)}\right)^k + (1-\beta)\left[P_{w_0} + c_{w_0}^2\left(\frac{(1-y)\tilde{\rho}_2}{(1-\beta)(1-\alpha)} - \rho_{w_0}\right)\right] \tag{24}$$

However, this equation should be expressed in a more friendly form. Now, we derive an expression for P_2 that only involves ρ_2 and y.

From Equation (23) and the definition of $\tilde{\rho}_2$, one can obtain the following:

$$P_2(\rho_2, y, \beta) = \beta \frac{P_{a_0}}{\rho_{a_0}^k} \left(\frac{y\rho_2}{\beta} \right)^k + (1-\beta) \left[P_{w_0} + c_{w_0}^2 \left(\frac{(1-y)\rho_2}{(1-\beta)} - \rho_{w_0} \right) \right] \tag{25}$$

Now, for β to vanish, one needs to express β upon ρ_2 and y. This is achieved by using the pressure equilibrium equation $P_a = P_w$. When developing the equations of states, it reads as follows:

$$\frac{P_{a_0}}{\rho_{a_0}^k} \left(\frac{y\rho_2}{\beta} \right)^k = P_{w_0} + c_{w_0}^2 \left(\frac{(1-y)\rho_2}{(1-\beta)} - \rho_{w_0} \right) \tag{26}$$

The solution β of this equation only depends on ρ_2 and y because the rest is constant. The problem is that this equation is implicit for β.

Let us try the particular case $k = 1$, which is simpler. Equation (26) becomes a second degree polynomial:

$$\beta^2 \ (P_{w_0} - c_{w_0}^2 \rho_{w_0}) - \beta \ \left(P_{w_0} + c_{w_0}^2 (1-y)\rho_2 - c_{w_0}^2 \rho_{w_0} + \frac{P_{a_0}}{\rho_{a_0}} y\rho_2 \right) + \frac{P_{a_0}}{\rho_{a_0}} y\rho_2 = 0 \tag{27}$$

of which the Δ reads as follows:

$$\Delta = \left(P_{w_0} + c_{w_0}^2 (1-y)\rho_2 - c_{w_0}^2 \rho_{w_0} + \frac{P_{a_0}}{\rho_{a_0}} (y\rho_2) \right)^2 - 4 \left(P_{w_0} - c_{w_0}^2 \rho_{w_0} \right) \frac{P_{a_0}}{\rho_{a_0}} (y\rho_2) \tag{28}$$

which leads to the expression for β as a function of ρ_2 and y:

$$\beta(\rho_2, y) = \frac{\left(P_{w_0} + c_{w_0}^2 (1-y)\rho_2 - c_{w_0}^2 \rho_{w_0} + \frac{P_{a_0}}{\rho_{a_0}} (y\rho_2) \right) \pm \sqrt{\Delta}}{2P_{w_0} - 2c_{w_0}^2 \rho_{w_0}} \tag{29}$$

Now, from Equation (25), one obtains the following:

$$\begin{aligned} P_2(\rho_2, y) = \frac{P_{a_0}}{\rho_{a_0}^k} y\rho_2 + & \left(\frac{P_{w_0} - c_{w_0}^2 \rho_{w_0} - c_{w_0}^2 (1-y)\rho_2 - \frac{P_{a_0}}{\rho_{a_0}} y\rho_2 \pm \sqrt{\Delta}}{2P_{w_0} - 2c_{w_0}^2 \rho_{w_0}} \right) \\ & \times \left[P_{w_0} + c_{w_0}^2 \left(\frac{(1-y)\rho_2}{(1-\beta)} - \rho_{w_0} \right) \right] \end{aligned} \tag{30}$$

This is a more friendly analytical expression for P_2 depending on ρ_2 and y only. However, this is only valid for $k = 1$. Equation (30) is plotted in Figure 3 for several fixed values of y.

The equation of state of fluid 2 in the case of $k = 1.4$ can be computed numerically.

2.4. Sound speed in the bubbly water (fluid 2)

In this section, the aim is to investigate the acoustic wave propagation in the mixture of air and water represented by fluid 2.

The definition of sound speed in fluid 2 at atmospheric pressure P_0 is as follows:

$$c_{2_0}^2 \equiv \left. \frac{\partial P_2}{\partial \rho_2} \right|_{\rho_{2_0}} \tag{31}$$

where the pressure in fluid 2 reads (Equation (14)):

$$P_2 = \beta P_a(\rho_a) + (1-\beta) P_w(\rho_w) \tag{32}$$

Let us emphasise that the sound speed is the speed of a linear pressure perturbation around a given reference state. Here, the reference state used is the standard state (P_{2_0}, ρ_{2_0}). This is the reason why subscript "0" is used.

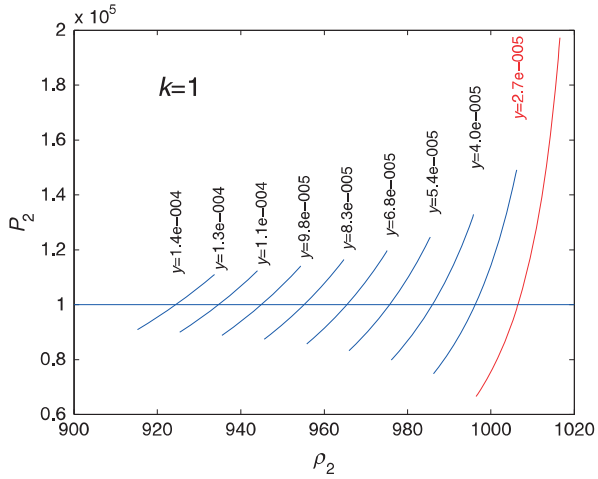

Figure 3. Resulting equation of state of fluid 2 for several fixed values of y.

Let us derive Equation (32) upon ρ_2:

$$\frac{\partial P_2}{\partial \rho_2} = \beta \frac{\partial P_a(\rho_a)}{\partial \rho_2} + (1-\beta)\frac{\partial P_w(\rho_w)}{\partial \rho_2} + (P_a - P_w)\frac{\partial \beta}{\partial \rho_2} \tag{33}$$

$$\frac{\partial P_2}{\partial \rho_2} = \beta \frac{\partial P_a(\rho_a)}{\partial \rho_a}\frac{\partial \rho_a}{\partial \rho_2} + (1-\beta)\frac{\partial P_w(\rho_w)}{\partial \rho_w}\frac{\partial \rho_w}{\partial \rho_2} + (P_a - P_w)\frac{\partial \beta}{\partial \rho_2} \tag{34}$$

As $\rho_a = \frac{y\rho_2}{\beta}$ and $\rho_w = \frac{(1-y)\rho_2}{1-\beta}$, Equation (34) becomes

$$\begin{aligned}\frac{\partial P_2}{\partial \rho_2} = {} & \frac{\partial P_a(\rho_a)}{\partial \rho_a} y \frac{\beta - \rho_2 \frac{\partial \beta}{\partial \rho_2}}{\beta} \\ & + \frac{\partial P_w(\rho_w)}{\partial \rho_w}(1-y)\frac{(1-\beta) + \rho_2 \frac{\partial \beta}{\partial \rho_2}}{(1-\beta)} + (P_a - P_w)\frac{\partial \beta}{\partial \rho_2}\end{aligned} \tag{35}$$

Now replacing y and $(1-y)$ by their expression upon ρ_a and ρ_w, we have the following equation:

$$\begin{aligned}\frac{\partial P_2}{\partial \rho_2} = {} & \frac{\partial P_a(\rho_a)}{\partial \rho_a}\rho_a\left(\frac{\beta}{\rho_2} - \frac{\partial \beta}{\partial \rho_2}\right) \\ & + \frac{\partial P_w(\rho_w)}{\partial \rho_w}\rho_w\left(\frac{(1-\beta)}{\rho_2} + \frac{\partial \beta}{\partial \rho_2}\right) + (P_a - P_w)\frac{\partial \beta}{\partial \rho_2}\end{aligned} \tag{36}$$

Now, to obtain sound speed as defined by Equation (31), one needs to take Equation (36) at the particular standard state (P_{2_0}, ρ_{2_0}). This leads to the introduction of the sound speeds in air $c_{a_0}^2 = \frac{\partial P_a}{\partial \rho_a}\Big|_{P_0}$ and water $c_{w_0}^2 = \frac{\partial P_w}{\partial \rho_w}\Big|_{P_0}$. Moreover, we use the fact that $P_a = P_w$, and we have the following expression for the sound speed in fluid 2:

$$c_{2_0}^2 = c_{a_0}^2\rho_{a_0}\left(\frac{\beta_0}{\rho_{2_0}} - \frac{\partial \beta_0}{\partial \rho_2}\Big|_{\rho_{2_0}}\right) + c_{w_0}^2\rho_{w_0}\left(\frac{(1-\beta_0)}{\rho_{2_0}} + \frac{\partial \beta_0}{\partial \rho_2}\Big|_{\rho_{2_0}}\right) \tag{37}$$

Now, we need an expression for $\frac{\partial \beta}{\partial \rho_2}\Big|_{\rho_{2_0}}$. It is obtained by rewriting the pressure equilibrium between air and water (Equation (16)) upon ρ_2 using relations (2) and (3):

$$\frac{P_0}{\rho_{a_0}^k}\left(\frac{y\rho_2}{\beta}\right)^k = P_0 + c_{w_0}^2\left(\frac{(1-y)\rho_2}{(1-\beta)} - \rho_{w_0}\right) \tag{38}$$

and by taking its derivative

$$\frac{P_0}{\rho_{a_0}^k} k \left(\frac{y\rho_2}{\beta}\right)^{k-1} \left(y\frac{\beta - \rho_2 \frac{\partial \beta}{\partial \rho_2}}{\beta^2}\right) = c_{w_0}^2 \left((1-y)\frac{(1-\beta) + \rho_2 \frac{\partial \beta}{\partial \rho_2}}{(1-\beta)^2}\right) \tag{39}$$

This leads to

$$\frac{\partial \beta}{\partial \rho_2} = \frac{\beta(1-\beta)^2 \frac{P_0}{\rho_{a_0}^k} k \left(\frac{y\rho_2}{\beta}\right)^{k-1} y - \beta^2 c_{w_0}^2 (1-y)(1-\beta)}{\beta^2 c_{w_0}^2 \rho_2 (1-y) + (1-\beta)^2 \frac{P_0}{\rho_{a_0}^k} k \left(\frac{y\rho_2}{\beta}\right)^{k-1} y\rho_2} \tag{40}$$

and at $\rho_2 = \rho_{2_0}$, we obtain

$$\left.\frac{\partial \beta}{\partial \rho_2}\right|_{\rho_{2_0}} = \frac{\beta_0(1-\beta_0)^2 \frac{P_0}{\rho_{a_0}^k} k \left(\frac{y\rho_{2_0}}{\beta_0}\right)^{k-1} y - \beta_0^2 c_{w_0}^2 (1-y)(1-\beta_0)}{\beta_0^2 c_{w_0}^2 \rho_{2_0} (1-y) + (1-\beta_0)^2 \frac{P_0}{\rho_{a_0}^k} k \left(\frac{y\rho_{2_0}}{\beta_0}\right)^{k-1} y\rho_{2_0}} \tag{41}$$

Replacing $\frac{y\rho_2}{\beta_0}$ by ρ_{a_0} (see Equation (1)) and $\frac{P_0}{\rho_{a_0}^k} k \rho_{a_0}^{k-1}$ by $c_{a_0}^2$ (derivative of Equation (19), we have the following equation:

$$\left.\frac{\partial \beta}{\partial \rho_2}\right|_{\rho_{2_0}} = \frac{\beta_0(1-\beta_0)^2 c_{a_0}^2 y - \beta_0^2 c_{w_0}^2 (1-y)(1-\beta_0)}{\beta_0^2 c_{w_0}^2 \rho_{2_0}(1-y) + (1-\beta_0)^2 c_{a_0}^2 y\rho_{2_0}} \tag{42}$$

Then replacing $(1-y)$ by $\frac{(1-\beta_0)\rho_{w_0}}{\rho_{2_0}}$ and y by $\frac{\beta_0 \rho_{a_0}}{\rho_{2_0}}$ (see Equation (1)) leads to the following equation:

$$\left.\frac{\partial \beta}{\partial \rho_2}\right|_{\rho_{2_0}} = \frac{\beta_0(1-\beta_0)}{\rho_{2_0}} \frac{c_{a_0}^2 \rho_{a_0} - c_{w_0}^2 \rho_{w_0}}{\beta_0 \rho_{w_0} c_{w_0}^2 + (1-\beta_0)\rho_{a_0} c_{a_0}^2} \tag{43}$$

Finally, by replacing expression (43) in Equation (37), one obtains the sound speed in fluid 2 as a function of β_0, ρ_2 and constants. It reads as follows:

$$\frac{1}{\rho_{2_0} c_{2_0}^2} = \frac{\beta_0}{\rho_{a_0} c_{a_0}^2} + \frac{(1-\beta_0)}{\rho_{w_0} c_{w_0}^2} \tag{44}$$

Thus, the expression for sound speed c_{2_0} in the model corresponds exactly to Wood's formula [9], which is a satisfying representation of the sound speed in gas–liquid mixtures.

3. NUMERICAL MODEL

The system of governing Equations (5)–(8), (15) and (16) is a model in which the relaxation process regarding pressure is assumed to be instantaneous. This model is numerically solved by using a second order Runge–Kutta scheme, in which the time step Δt^n is adapted at each iteration to satisfy a CFL condition.

Within each of the two stages of the Runge–Kutta scheme, a fractional-step method with two steps is used. In the first step of this fractional step method, called the transport step, the relaxation is assumed to be frozen. Thus, the Equations (15) and (16) are replaced by transport equations for α and β (see [12]) so that the system becomes system (45), which is prone to lead to a hyperbolic problem and thus easier to solve (see [13] for the detailed Riemann problem solution). In the second step, the pressure is 'released' by setting an infinite relaxation speed. This means that the solution obtained at the transport step is 'relaxed' to restore the pressure equilibrium. This step is called the relaxation step. To sum up, using this fractional-step method amounts to solving an approximation of the system (5)–(8), (15) and (16), firstly, by considering an infinite relaxation time and transporting the variables, and secondly, by considering a zero relaxation time. Finally, the approximation we

make is that the overall relaxation time is equal to the time step. So this method is only first order accurate in time. This is not a severe limitation as the numerical method is explicit, and the time step will be small anyway because of the stability condition.

It is relevant to notice that because of the numerical method both fluids 1 and 2 must be present everywhere in the domain, at least in very small proportions.

3.1. Transport step

During this step, the system of conservation equations associated with the model (Equations (5)–(8)) and the supplementary transport equations for α and β, but with zero right members, are integrated including the source terms from volume forces and viscous effects:

$$\frac{\mathrm{d}}{\mathrm{d}t}\begin{pmatrix} \alpha \\ \beta \\ \tilde{\rho}_1 \\ \tilde{\rho}_2 \\ \tilde{\rho}_2 y \\ \rho \underline{V} \end{pmatrix} = \begin{pmatrix} 0 \\ 0 \\ 0 \\ 0 \\ 0 \\ \nabla.\tau^D + \underline{F} \end{pmatrix} \tag{45}$$

where $\frac{d}{dt}$ represents the operator $\frac{\partial}{\partial t} + \nabla.$. This is the equivalent to temporarily considering a frozen relaxation (infinite relaxation time or zero relaxation speed). The system that has to be integrated is thus a system of balance equations, which, for 3D Cartesian frame, has the following form:

$$\frac{\partial W}{\partial t} + \frac{\partial F}{\partial x} + \frac{\partial G}{\partial y} + \frac{\partial H}{\partial z} = S \tag{46}$$

W being the vector of conservative variables, F the vector flux along x, G the flux along y, H the flux along z and S the source term including viscous forces:

$$S = S^{\mathrm{visc}} + S^{\mathrm{ext}} = \nabla.\left(\tau^D\right) + \rho \underline{g} \tag{47}$$

This system of conservation laws is discretised using the finite volume method over a Cartesian grid (the code is able to deal with unstructured grid, but for the sake of simplicity, we present the methods for a Cartesian grid). The integration volume, which is the volume of the cell, reads as follows:

$$C_{i,j,k} = \left[x_{i-\frac{1}{2}}, x_{i+\frac{1}{2}}\right] \times \left[y_{j-\frac{1}{2}}, y_{j+\frac{1}{2}}\right] \times \left[z_{k-\frac{1}{2}}, z_{k+\frac{1}{2}}\right] \tag{48}$$

The numerical unknowns are $W_{i,j,k}$ defined by the volume-averaged continuous variables:

$$W_{i,j,k} = \frac{1}{|C_{i,j,k}|} \int_{C_{i,j,k}} W \mathrm{d}V \tag{49}$$

The source term quantity $S_{i,j,k}$ is defined as

$$S_{i,j,k} = \frac{1}{|C_{i,j,k}|} \int_{C_{i,j,k}} S \mathrm{d}V \tag{50}$$

The volume integration of the system (46) using Ostrogradski theorem leads to the following semi-discrete scheme:

$$\frac{\partial W_{i,j,k}}{\partial t} + \sum_{\mathrm{faces}} \frac{1}{|C_{i,j,k}|} \int_{\mathrm{face}} \left(F\mathbf{e}_x + G\mathbf{e}_y + H\mathbf{e}_z\right).\mathbf{n}_{\mathrm{face}} \mathrm{d}S \tag{51}$$

where the sum $\sum_{\mathrm{faces}}$ refers to the faces of the cell where the integral $\int_{\mathrm{face}}$ concerns each one of these faces. By assuming these fluxes to be constant over a face, one obtains the following:

$$\int_{\mathrm{face}} \left(F\mathbf{e}_x + G\mathbf{e}_y + H\mathbf{e}_z\right).\mathbf{n}_{\mathrm{face}} \mathrm{d}S \approx \left(f\mathbf{e}_x + g\mathbf{e}_y + h\mathbf{e}_z\right).\mathbf{n}_{\mathrm{face}} |F| \tag{52}$$

where f, g, and h are numerical flux functions depending on the unknowns $W_{i,j,k}$ in the cells on both sides of the considered face:

$$\frac{\partial W_{i,j,k}}{\partial t} = S_{i,j,k} - \left(\frac{f_{i+\frac{1}{2},j,k} - f_{i-\frac{1}{2},j,k}}{\Delta x_i} + \frac{g_{i,j+\frac{1}{2},k} - g_{i,j-\frac{1}{2},k}}{\Delta y_j} + \frac{h_{i,j,k+\frac{1}{2}} - h_{i,j,k-\frac{1}{2}}}{\Delta z_k} \right) \quad (53)$$

where Δx_i, Δy_j and Δz_k are the local space steps in each direction and where $f_{p,j,k}$ refers to the flux through the face of abscissa x_p on the jth line of the grid. The fluxes $f_{i+\frac{1}{2},j,k}$, $g_{i,j+\frac{1}{2}}$ and $h_{i,j,k+\frac{1}{2}}$ through considered faces located respectively at $i+\frac{1}{2}$, $j+\frac{1}{2}$ and $k+\frac{1}{2}$ are numerically approximated by the numerical flux functions $f(W_{i,j,k}, W_{i+1,j,k})$, $g(W_{i,j,k}, W_{i,j+1,k})$ and $h(W_{i,j,k}, W_{i,j,k+1})$, which depend on the states in the cells on both sides of the considered faces.

3.2. Numerical scheme for the diffusion term

The scheme used to discretise the viscous term in the right side of the momentum equation of the model is a classical finite difference scheme on a Cartesian grid (see [7] for more detail). The treatment for the sources terms is thus explicit.

However, as the explicit characteristic of the scheme is restricting in CPU terms, a low-Mach approximation is being developed.

Flux estimation First, it is important to consider a scheme that ensures mass positivity. Among the exact schemes on stationary contact discontinuities, the Godunov scheme presents a small numerical diffusion.

The Godunov scheme consists in using, as numerical flux function, the flux corresponding to the exact solution of the Riemann problem associated with the model, in which the states in the cells on both sides of the interface are those of the previous time step:

$$f_{i+\frac{1}{2},j,k} = f(W_{i,j,k}, W_{i+1,j,k}) = F\left(W^R(0; W_l, W_r) \right) \quad (54)$$

where W^R is the solution of the Riemann problem associated with the model and with the left and right conditions W_l and W_r. The numerical fluxes $g_{i,j+\frac{1}{2},k}$ and $h_{i,j,k+\frac{1}{2}}$ are estimated the same way.

In the computation of these fluxes, we first need the densities at the face, $\rho_{1\text{face}}$ and $\rho_{2\text{face}}$. They are given by the resolution of the Riemann problem corresponding to the model. Then, the total pressure at the face is needed. It reads $P = \alpha_1 P_1 + \alpha_2 P_2$. Therefore, P_1 and P_2 are needed at the considered face. P_1 depends on $\rho_{1\text{face}}$ through the equation of state of fluid 1 (Equation (17)). But the expression of P_2 in Equation (24) cannot be used directly because the Godunov scheme in the code has been developed to deal with linear equations of state. Thus, we use a local and instantaneous linear approximation equation of state of fluid 2:

$$P_2 = P_{2,\text{ref}} + c^2_{2,\text{ref}} (\rho_{2\text{face}} - \rho_{2,\text{ref}}) \quad (55)$$

where $\rho_{2\text{face}}$ is given by the resolution of the Riemann problem. However, the reference state $(P_{2,\text{ref}}, \rho_{2,\text{ref}}, c_{2,\text{ref}})$, which has to be local (for each cell) and instantaneous (for each time step of the Runge–Kutta method), must be approximated. For $P_{2,\text{ref}}$, we take the arithmetic mean of the pressures at the previous time step in the cells at the left and right sides of the considered face: $P_{2,L}$ and $P_{2,R}$. In the same way, for $\rho_{2,\text{ref}}$, we take the arithmetic mean of the densities at the previous time step in the cells at the left and right sides of the considered face: $\rho_{2,L}$ and $\rho_{2,R}$.

Now, for $c_{2,\text{ref}}$, we chose to take the arithmetic mean of the sound speed associated with the state in the cells at the left and right sides of the considered face at the previous time step: $c_{2,L}$ and $c_{2,R}$.

$c_{2,L}$ is computed through the equation defining the sound speed in fluid 2 (Equation (44)) using the state at the previous time step in the cell at the left side of the considered face: $(\rho_{2,L}, \beta_2, P_{2,L}, \rho_{a,L}, c_{a,L}, \rho_{w,L}, c_{w,L})$, where $c_{a,L}$ is computed through the equation of state of fluid a, $c_{a,L} = \sqrt{\frac{k\, P_{2,L}}{\rho_{a,L}}}$, which is the derivative of Equation (19) taken in the cell at the left side of the face, and where $c_{w,L}$ is equal to the constant $c_{w,0}$ (as in the linear equation of state of fluid w, Equation (21)).

In the same way, $c_{2,R}$ is computed although Equation (44) using the state at the previous time step in the cell at the right side of the considered face: $(\rho_{2,R}, \beta_2, P_{2,R}, \rho_{a,R}, c_{a,R}, \rho_{w,R}, c_{w,R})$.

The second order in space is obtained, thanks to the MUSCL method along with the slope limiter called monotonised central with a steepness set to 1.8.

At this stage, given the conservative variables at time t_n, the scheme allows to compute the conservative variables at time t_{n+1}:
$W^{n+1} =^t (\rho\alpha, \beta, \tilde{\rho}_1, \tilde{\rho}_2, \tilde{\rho}_2 y, \rho\underline{V})$, which all depend on the 'natural variables' at time t_{n+1}: $V^n =^t (\alpha, \beta, \rho_1, \rho_2, y, \underline{V})$. However, the volume fractions obtained at the end of this step do not correspond to the pressure equilibrium. It is thus necessary to update them through the relaxation step.

3.3. Relaxation step

After the transport step, the conservative variables $\tilde{\rho}_1$, $\tilde{\rho}_2$, $\tilde{\rho}_2 y$ et $\rho\underline{V}$ are known. It is then necessary to compute values of α and β that satisfy the pressure equilibria (16) and (15). This will allow us to compute the natural variables $\rho_1 = \frac{\tilde{\rho}_1}{\alpha}$, $\rho_2 = \frac{\tilde{\rho}_2}{1-\alpha}$, $\rho_a = \frac{\tilde{\rho}_a}{\beta}$ and $\rho_w = \frac{\tilde{\rho}_w}{1-\beta}$ and the pressures. This step is the second step of the fractional-step method performed here. The following system is solved with ϵ tending towards zero:

$$\frac{\mathrm{d}}{\mathrm{d}t}\begin{pmatrix} \alpha \\ \beta \\ \tilde{\rho}_1 \\ \tilde{\rho}_2 \\ \tilde{\rho}_2 y \\ \rho\underline{V} \end{pmatrix} = \begin{pmatrix} \frac{P_2 - P_1}{\epsilon} \\ \frac{P_w - P_a}{\epsilon} \\ 0 \\ 0 \\ 0 \\ 0 \end{pmatrix} \tag{56}$$

It is obvious that only α and β vary through this step. The first two equations are equivalent to finding α and β such as $P_1 = P_2$ and $P_a = P_w$, because ϵ tends towards zero.

For our equations of state (Equations (18), (20) and (22)), the system formed by the pressure equilibrium equations (Equations (15) and (16)) cannot be solved explicitly, and a numerical scheme is used instead to compute the equilibria volume fractions.

Firstly, the pressure-equilibrium equation between air and water within fluid 2 (Equation (16)) reads, using equations of state (20) and (22) involving conservative variables:

$$\frac{P_0}{\rho_{a_0}^k}\left(\frac{y\tilde{\rho}_2}{\beta(1-\alpha)}\right)^k = P_0 + c_{w_0}^2\left(\frac{(1-y)\tilde{\rho}_2}{(1-\beta)(1-\alpha)} - \rho_{w_0}\right) \tag{57}$$

Equation (57) involves the unknowns α and β, constants $(P_0, \rho_{a_0}, c_{w_0}, \rho_{w_0}, k)$ and conservative variables $\tilde{\rho}_2$ and $\tilde{\rho}_2 y$ that have been computed during transport step. Thus, Equation (57) constitutes a first equation that will be of use to compute α et β. The left part of Equation (57) is a decreasing function, and the right part is an increasing function, then the solution β is unique.

Secondly, the other equation involving α and β is the pressure equilibrium equation between fluids 1 and 2 (Equation (15)). In Equation (15), the computation of P_1 is easily achieved by using the equation of state of fluid 1 (Equation (18)). However, the expression of P_2 through Equation (24) is too complex to be used here. Instead, we replace P_2 by P_w, which are exactly equal as all the pressures have been relaxed at the previous time step. Indeed, $P_2 = \beta P_a + (1-\beta)P_w$ (Equation (14)) and $P_a = P_w$ (Equation (16)), thus $P_2 = \beta P_a + (1-\beta)P_w = P_w$. Then, we rewrite the pressure equilibrium between fluids 1 and 2 (15) in:

$$P_1 = P_w \tag{58}$$

This trick is useful because P_w has the advantage of being simple linear equation of state. Now, pressure equilibrium between fluids 1 and 2 reads, by replacing with equations of state (18) and (22):

$$P_{1_0} + c_{1_0}^2 \left(\frac{\tilde{\rho}_1}{\alpha} - \rho_{1_0} \right) = P_{w_0} + c_{w_0}^2 \left(\frac{(1-y)\tilde{\rho}_2}{(1-\beta)(1-\alpha)} - \rho_{w_0} \right) \tag{59}$$

Equation (59) constitutes the second necessary equation for computing α and β. The relation between β and α through Equation (59) can be found explicitly.

The computation of α and β through Equations (57) and (59) is achieved by using a Newton–Raphson method generalised to systems of two equations.

4. MODEL VALIDATION

4.1. Acoustic wave propagation in a bubbly liquid

The aim of this section is to analyse the accuracy of the code in the modelling of an acoustic-wave propagation in a homogeneous bubbly liquid. For this purpose, we measure the speed of sound and the attenuation of a pressure wave in a mixture of air and water.

4.1.1. Set-up. The chosen reference case is the experiment carried out by [14]. Air bubbles are injected at the bottom of a water-filled cylinder (diameter 7.62 cm) and rise towards the free surface. The top of the cylinder is open to the atmosphere. A transducer, placed at the bottom of the column, generates pressure waves propagating towards the free surface, located 1.80 m above the transducer. The pressure wave that is generated at the bottom of the column propagates upwards and is partly reflected at the free surface. Then, it propagates back downwards and is reflected at the bottom. Then, it is reflected back and forth and is damped on both upward and downward courses. Thus, a quasi-stationary damped wave is obtained. Sound pressure measurements are made along the centre of the column with a movable hydrophone.

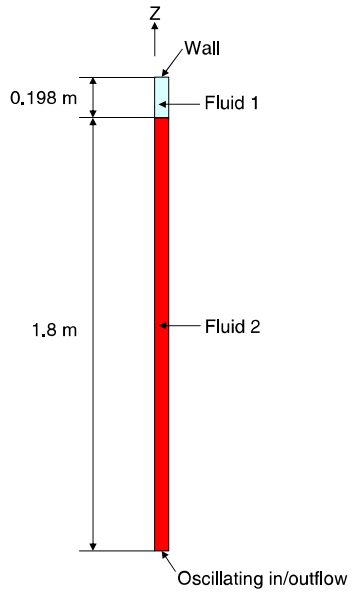

Figure 4. Numerical set-up corresponding to [14] case.

The corresponding numerical set-up is represented in Figure 4. Let us note that the subscript '0' is used for values taken at atmospheric pressure. The numerical domain is filled with a mixture of air and water (fluid 2), up to 1.80 m above the bottom as in the experiment, and with pure air (fluid 1) above. This set-up allows us to represent the presence of the atmosphere above the free surface but over a small vertical distance to avoid adding too many computation cells. The upper boundary condition is a wall because the code does not allow the use of an open condition as in the experience. We verified that it does not introduce perturbations in the flow. At the side boundaries, symmetry conditions are used, and only one cell is used in the horizontal direction to reproduce a

one-dimensional problem. Let us notice that because of the numerical method in the practice, an infinitesimal quantity of fluid 1 must be set in the fluid-2-filled part and vice versa. Therefore, the initial spatial distribution of fluid-1 volume fraction at atmospheric pressure is written as follows:

$$\alpha_0(z) = \begin{cases} 10^{-9} & \text{for} \quad 0 < z < 1.8 \\ 1 - 10^{-9} & \text{for} \quad 1.8 < z < 1.998 \end{cases} \tag{60}$$

Fluid 1 is an approximation of air obeying the linear equation of state (17) with $\rho_{1_0} = 1.33\ \text{kg.m}^{-3}$ and $c_{1_0} = 340\ \text{m.s}^{-1}$.

Fluid 2 is a mixture of air (fluid a, whose density is $\rho_{a_0} = 1.33\ \text{kg.m}^{-3}$, and sound speed is $c_{a_0} = 340\ \text{m.s}^{-1}$) and water (fluid w, which density is $\rho_{w_0} = 1027\ \text{kg.m}^{-3}$, and sound speed is $c_{w_0} = 1500\ \text{m.s}^{-1}$). Fluid-a (air) mass fraction y is uniformly set to $y = 4.89795\ 10^{-7}$. Thus, close to the free surface, where the pressure is the atmospheric pressure, the air volume fraction is $\beta_0 = 3.77\ 10^{-4}$, which is one of the values used by [14]. It is important to notice that because of hydrostatic pressure variation, $\beta_0(x)$ decreases from the free surface to the bottom.

The bottom boundary is an oscillating in/outflow condition, which allows us to generate a pressure oscillation at the bottom of the numerical domain over the whole duration of the simulation. The amplitude of the pressure wave is small (around 3 Pa) to stay within the acoustic limit. The frequency of the oscillations are varied within the [374–12 384] Hz interval.

Figure 5 shows an example of an instantaneous pressure field obtained for a forcing frequency of 2012 Hz. The free surface being located at $z = 1.80$ m, one can see that the pressure wave front has not reached the free surface yet. When it does, it will be reflected partially, and the reflected wave will superimpose itself with the incident one. One can observe a slight decrease in the wave amplitude with altitude z attributable to a damping effect.

To characterise the quasi-stationary wave, the same method as in [14] is used, which is to analyse the root mean square (RMS) pressure fluctuation field $P_{\text{RMS}}(z)$:

$$P_{\text{RMS}}(z) = \sqrt{\overline{\left(P(z,t) - P_{\text{hyd}}(z)\right)^2}} \tag{61}$$

where P is the pressure, P_{hyd} is the hydrostatic component of the pressure and $\overline{A(t)}$ is the time average of $A(t)$ (here, over the duration of the simulation .09 s). Figure 6 shows an example of $P_{\text{RMS}}(z)$. $P_{\text{RMS}}(z)$ oscillates in space, which is related to the stationary characteristic of the wave. But P_{RMS} does not reach zero, which is due to the residual propagative part in this quasi-stationary signal. In Figure 6, for a 2012 Hz forcing, the amplitude of P_{RMS} oscillations increases with z. The amplitude is larger, closer to the free surface than to the bottom because the wave reflected on the

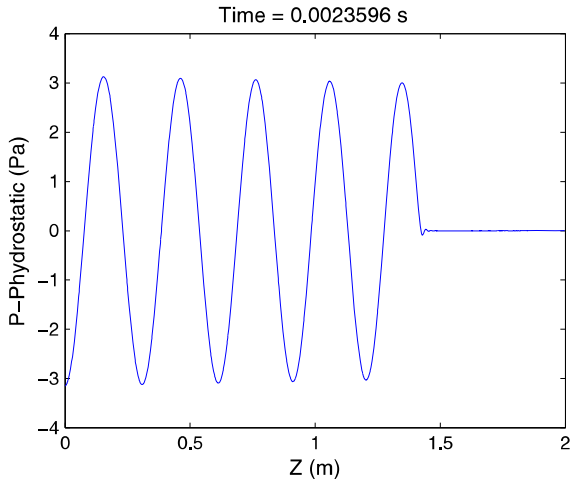

Figure 5. Example of instantaneous pressure field for 2220 cells and 2012 Hz. The bottom of the column where the wave is generated is on the left-hand side.

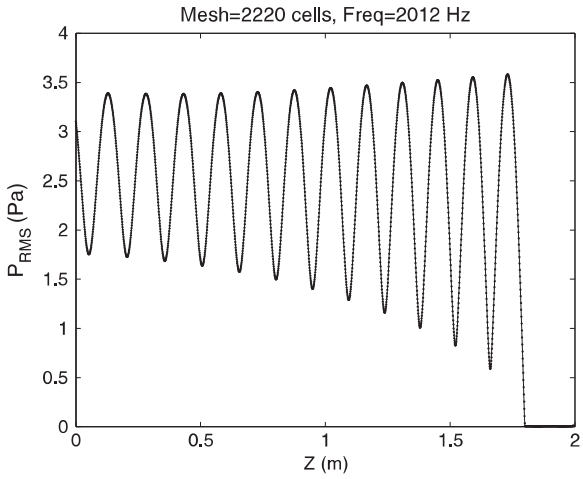

Figure 6. Example of root mean square pressure field for 2220 cells and 2012 Hz.

free surface superimposes with the incident upward wave. However, this is not always the case; as in some cases, the amplitude decreases with z.

Figure 6 shows that the pressure wave is almost entirely reflected at the free surface, because P_{RMS} is zero above the free surface.

The shape of P_{RMS} indicates that the pressure wave is almost steady near the free surface because of the almost full reflection. However, the pressure wave is far from stationary near the bottom of the column because the upward pressure wave is superimposed to the damped reflected wave propagating downwards.

4.1.2. Sound speed. The computed sound speed in the mixture is compared with analytical results and experimental data for different air contents and different frequencies. The aim is to show that the sound speeds computed by the numerical model are accurate.

Figure 7(a) shows a plot of sound speed at a constant air volume fraction $\beta = 3.77\ 10^{-4}$ and at frequencies well below bubble resonance frequency $f_0 = 2738$ Hz estimated theoretically by [15]. Let us note that we do not investigate frequencies close to bubble resonance frequency because our model is unable to represent the bubble resonance phenomenon. The sound speed is almost independent of frequency as expected from the theory [15, see] and close to the results from the models of [9] and [15] and experimental sound speed values.

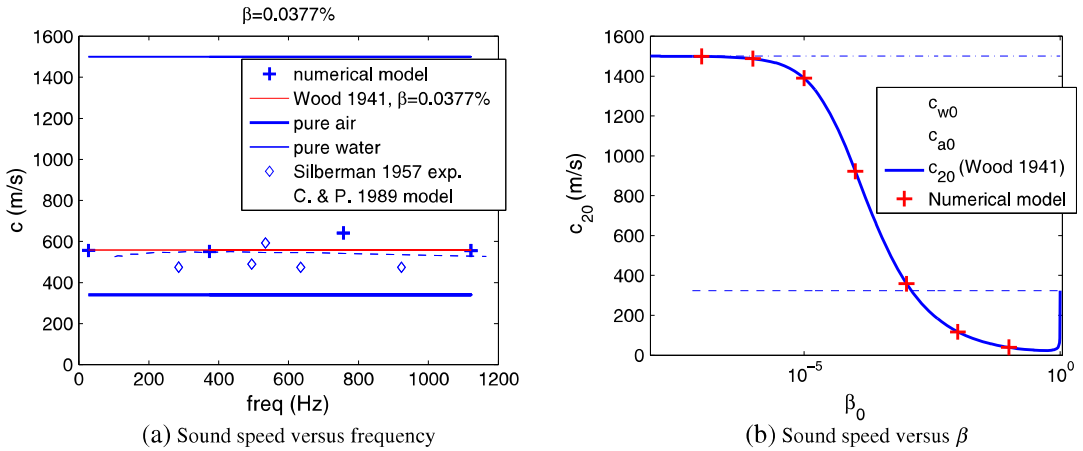

(a) Sound speed versus frequency

(b) Sound speed versus β

Figure 7. Sound speed versus frequency and air content.

Figure 7(b) shows a plot of sound speed versus air volume fraction β. This graph shows a fair agreement of sound speed with Wood's law.

This test shows that, far from the bubble resonance frequency, the numerical model represents the speed of sound in a mixture of air and water with good accuracy.

4.1.3. Wave attenuation. This section aims to present the ability of the numerical model to account for the viscous attenuation of an acoustic wave. In a mixture of air and water, the presence of bubbles can severely increase dissipative processes. Indeed, it has been shown in the literature that pressure waves at frequencies close to bubble resonance frequency experience a larger dissipation (cf. [15]). However, as the numerical model developed here does not take into account the bubbles as separated entities, we do not expect such an increase in the dissipation for frequencies around bubble resonance frequency.

Estimation of wave attenuation The wave attenuation at a node or antinode in Figure 6 is estimated by [14]:

$$\mathrm{Att} = \frac{4\,f}{n\,c}\, a\tanh\left(\frac{P_{\mathrm{RMSmin}}}{P_{\mathrm{RMSmax}}}\right) \tag{62}$$

where f is the temporal frequency, c is the sound speed, n is the number of quarter wavelength from the free surface to the node or antinode in question (cf. Figure 6). $P_{RMS\,\mathrm{min}}$ and $P_{RMS\,\mathrm{max}}$ are the min and max of P_{RMS} at the considered node or antinode, obtained by assuming linear variation of the maxima of P_{RMS} and the minima of P_{RMS} over each half-wavelength interval. For instance, when considering a node, $P_{\mathrm{RMS\,min}}$ is the value of P_{RMS} at the node, and P_{RMSmax} is found by linear interpolation between the values of P_{RMS} and the two neighbouring antinodes.

Numerical attenuation attributable to the grid resolution There is a difference between the physical attenuation and the numerical attenuation. To estimate the required resolution to keep the numerical attenuation smaller than the physical attenuation, different mesh refinements are used for a set of physical parameters, for which the pressure wavelength equals the domain height (mode 1), is investigated. The value of the attenuation defined by Equation (62) is plotted in Figure 8 for several grid resolutions. The attenuation intensity decreases exponentially as the resolution (grid points per wavelength) is increased and reaches a plateau that corresponds to the physical attenuation. Figure 8 shows that the attenuation is close to the physical attenuation provided that the resolution is at least 50 cells per wavelength.

Influence of frequency We showed in the previous section that, provided a sufficient resolution, which is the case in the present section, the measured attenuation is the physical one.

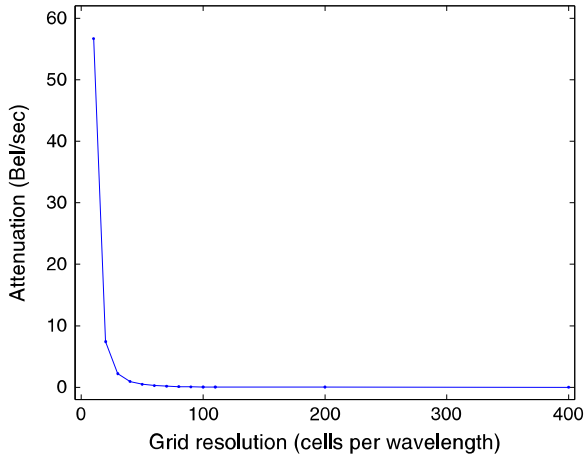

Figure 8. Wave attenuation versus grid resolution for a standing linear pressure wave, $\beta = 3.77 \times 10^{-4}$.

Figure 9 represents the attenuation Att (Equation (62)) versus the elevation in the column for a forcing frequency of 2012 Hz. This figure shows that the attenuation strongly increases with the altitude from the bottom to the free surface.

In Figure 10, attenuation is plotted versus wave frequency. One should notice that [14] do not mention if they consider minimum, maximum, average over the column or other values for the attenuation estimation. To circumvent this problem, we plotted in Figure 10, vertical bars that extend from the minimum to the maximum computed attenuation values for a given frequency. The green bars are for the coarse mesh (222 cells), which was used for the lower frequency values. For higher frequencies, we used a finer mesh (2220 cells, represented by the blue bars) to provide a resolution high enough to respect the criterion of at least 50 cells per pressure wave length established in the previous section.

One can see that theoretical and experimental attenuations first increase gently with frequency (200–2000 Hz). Then it experiences a jump (2000 Hz) and reaches its maximum around the fundamental bubble resonance frequency $f_0 = 3.26$ kHz. Then, it decreases strongly (3000–9000 Hz) and then returns to moderate values (10 000–100 000 Hz). The theoretical model of [15] is in good agreement with the experiment of [14].

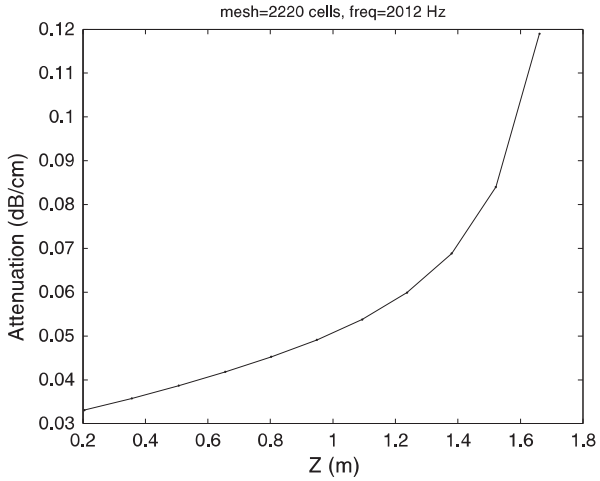

Figure 9. Attenuation versus altitude, $\beta = 3.77 \times 10^{-4}$, frequency = 2012 Hz.

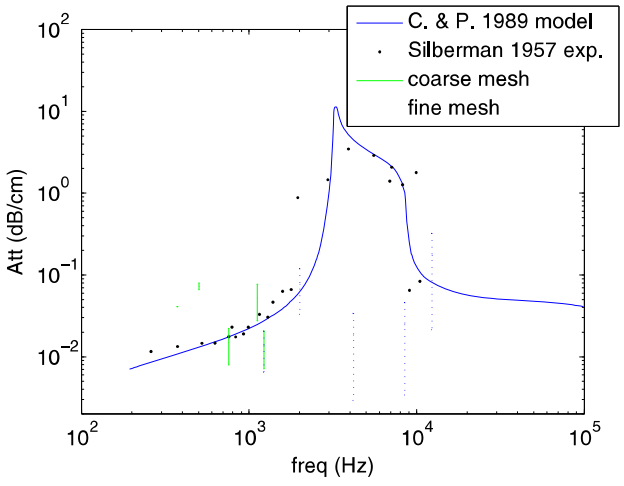

Figure 10. Attenuation versus frequency for $\beta = 3.77 \times 10^{-4}$.

The numerical results are in reasonable agreement with both experimental and theoretical data for frequencies below and above the high-dissipation frequency range (2000–9000 Hz), where the attenuation is underestimated as expected. Let us note that for the frequency 1228 Hz, both results from the coarse and fine meshes are plotted, and they are superimposed. Thus, this confirms that the attenuation considered here is the physical attenuation.

4.2. Validation 2: Shock tube

Shock waves may happen in the aerated water after a wave impact on a wall [16]. Therefore, it is necessary to assess the ability of the numerical model to properly represent the propagation of a shock wave. For that purpose, the classic shock tube-test case is used. We will investigate values of standard air volume fraction ranging between 0.0001 and 0.05 and compare the computed pressure with an analytical solution to evaluate the accuracy of the numerical model.

We recall that the configuration is a one-dimensional tube divided by a membrane into two inner parts. The left part is initially filled with a fluid at high pressure, and the right part with another fluid at low pressure, then the membrane is broken.

We consider a shock tube, whose both parts are filled with a mixture of air and water (fluid 2), with a given air mass fraction. (In practice, fluid 1 is almost absent: $\alpha = 10^{-9}$). The initial pressure is $P_{iL} = 10^6\ Pa$ in the left part and $P_{iR} = 10^5\ Pa$ in the right part. The air mass fraction y is identical in both left and right parts of the tube. We investigate five values for the air mass fraction. For the first case, the air mass fraction is set to $y = 1.3118\,10^{-5}$ in both parts, which corresponds to an initial air volume fraction of $\beta_{iR} = 0.01$ in the right part and of $\beta_{iL} = 0.00195$ in the left part. The initial physical parameters for this first case are reported in Table I.

Numerical results are compared with the mathematical model recently proposed by [17], which provides Hugoniot type shock relations for mixtures, allowing us to perform a simple comparison to our model. It is important to notice that Saurel *et al.*'s model [17] is not equivalent to our numerical model. Indeed, in their model, both fluids are represented by stiffened gas equations of state. Whereas in our numerical model, the equations of state are a polytropic equation for fluid a and a linear equation for fluid w. Moreover, [17] use an energy conservation equation. Whereas our model only represents dynamics as thermal effect are assumed to be non dominant in wave-impact problems. But this is the closest model, with an analytical solution, for a gas–liquid shock tube we found in the literature. Some discrepancies can thus be expected around the contact discontinuity and will be discussed succeedingly.

The results are shown in Figure 11.

The shock wave location ($Z = 0.1142$ m for the considered time) is very accurate which means that the shock speed is properly computed.

The solution between the rarefaction wave and the shock wave ($-0.1844\,m < Z < 0.1142\,m$) is globally accurate. One can note a slight discrepancy at the right of the contact discontinuity ($0 < Z < 0.1142\,m$) particularly in the graphs for β (Figure 11(e)), density of fluid a (Figure 11(c)) and density of fluid 2 (Figure 11(f)). Indeed, in the analytical model densities depend on the internal energy (through Stiffened Gas equation), which is not the case in the numerical model. And as the internal energy is not continuous at the interface, the densities also undertake a jump.

Let us notice that although the left and right internal energies are initially different, they would have reached the same value if the thermodynamic paths undertaken by the left and right parts of the interface were the same. But it is not the case, as a shock is a highly dissipative process in which the loss of kinetic energy generates an increase in heat and therefore in internal energy. This explains the jump in densities at the contact discontinuity in the analytical solution.

Table I. Shock-tube initial parameters for the first case.

	$P_i\ (Pa)$	y	ρ_{ai} (kg.m^{-3})	ρ_{wi} (kg.m^{-3})	β_i	u_i (m.s^{-1})
Left	10^6	$1.3118\ 10^{-5}$	6.908	1027.4	0.00195	0
Right	10^5	$1.3118\ 10^{-5}$	1.33	1027	0.01	0

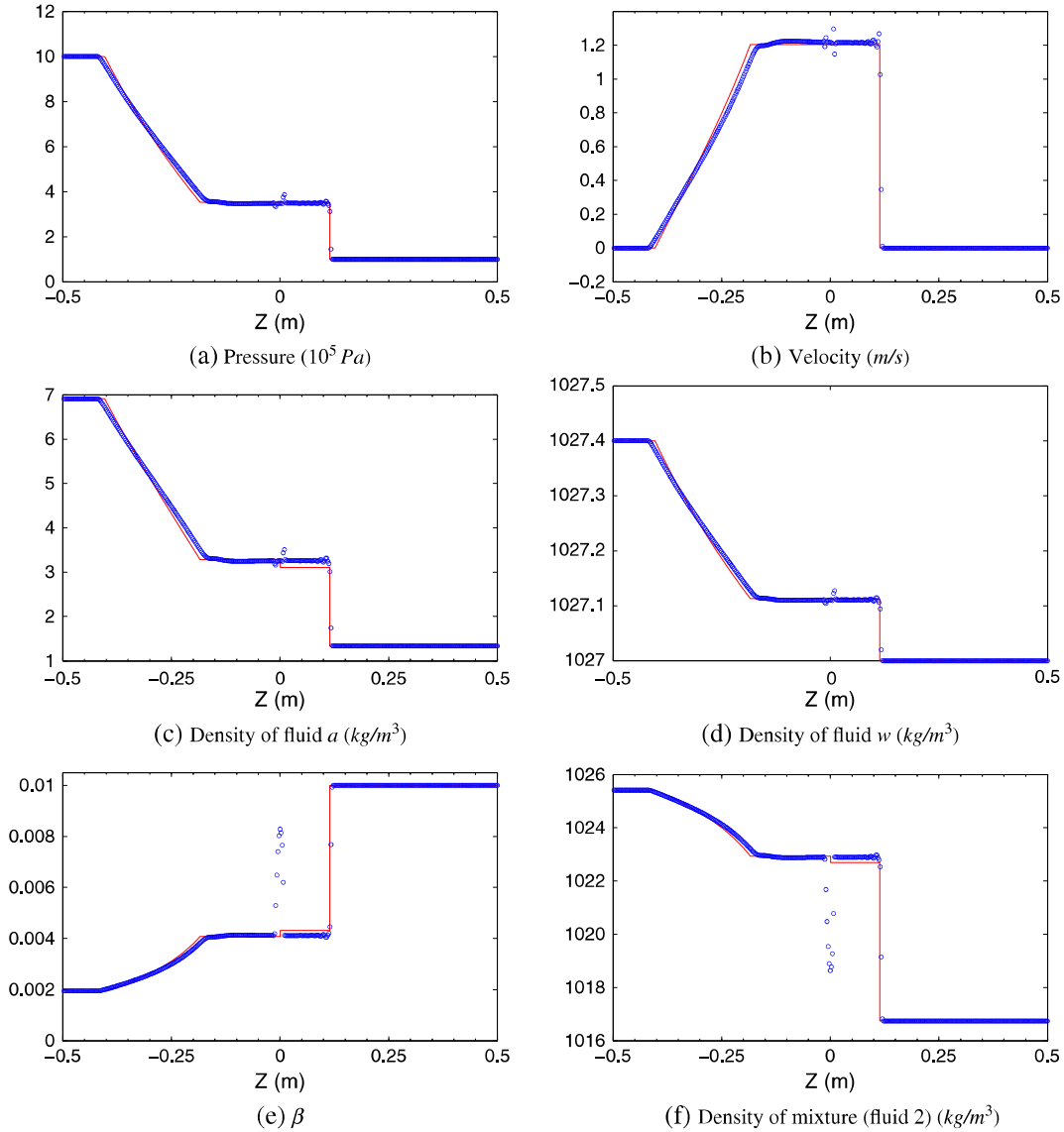

(a) Pressure ($10^5\ Pa$) (b) Velocity (m/s)

(c) Density of fluid a (kg/m^3) (d) Density of fluid w (kg/m^3)

(e) β (f) Density of mixture (fluid 2) (kg/m^3)

Figure 11. Comparison of a numerical simulation of the mixture shock tube with 800 cells to the analytical solution, for $P_L/P_R = 10$ and $\beta_0 = 0.01$, Time=$5.5137 \times 10^{-4}\ s$.

One can notice oscillations at the contact discontinuity, in particular in Figure 11(e) and (f). This is certainly due to the approximation we used in the Riemann solver. Indeed, the Godunov method we implemented relies on a linear equation of state, so we made the assumption that the previous time step state is close enough to current time step state to linearly extrapolate the current state from it. This generates an unwanted oscillation at the contact discontinuity.
However, as the main interest of this study is to characterise pressure field dynamics, this is not of first importance.

One can also notice (e.g. Figure 11(a)) that the rarefaction wave has a slightly larger spatial extension than in the analytical solution. The rarefaction front is thus less steep, which is characteristic of a numerical diffusion process.

Then, the same test case for different values of air mass fractions were performed. We focus on the pressure as this is what is of interest in this study (Figure 12). The agreement with the analytical solution is good whatever the air mass fraction, even though some slight spurious oscillations around the interface are observed, particularly in Figure 12(b).

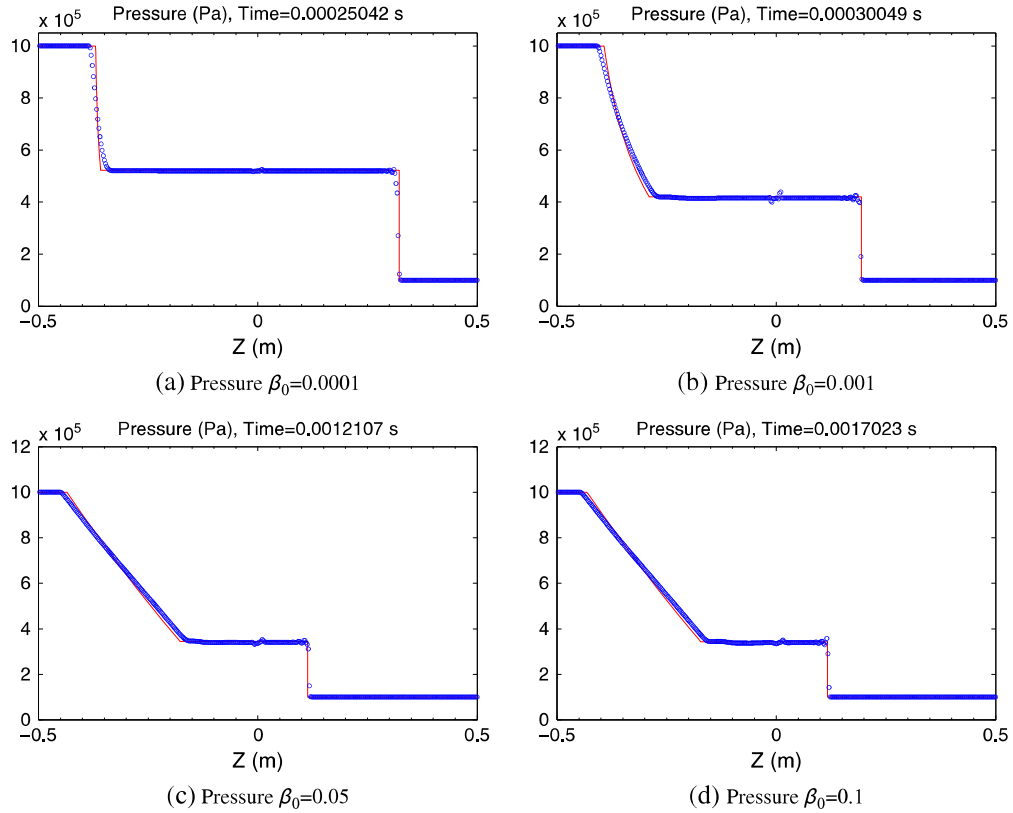

(a) Pressure β_0=0.0001 (b) Pressure β_0=0.001

(c) Pressure β_0=0.05 (d) Pressure β_0=0.1

Figure 12. Comparison of the numerical simulation of the mixture shock tube with 800 cells to the analytical solution, for $P_L/P_R = 10$ and different values of β_0.

4.3. Validation 3: Deep water breaking Stokes Wave at the incompressible limit

This section aims to validate the numerical model for a breaking wave configuration. We chose a Stokes wave breaking in deep water. The representation of complex free surface dynamics by our code is compared with an incompressible numerical model on the basis of a one-fluid model with a volume Of fluid method proposed by [18]. The simulation is initialised with a propagating Stokes wave solution, with fluid 1 representing air above free surface, and fluid 2 representing liquid below free surface. The steepness of the wave is chosen so that the breaking process is expected to occur soon. To properly compare it with the incompressible model, our model is run in the limit of fluid 2 being pure water. This is achieved by setting fluid-'a' mass fraction (air) within liquid phase (fluid 2) to almost zero, $y = 1.2987.10^{-10}$, which corresponds at atmospheric pressure to a volume fraction of $\beta = 10^{-7}$. It is important to notice that our methods being explicit, we set the sound speeds in equations of state of fluid 'w' and fluid 1 to 70 m/s to limit the computation time. This value however verifies a criterion for incompressibility defined by [7]. The incompressible Navier–Stokes model is run on a uniform 512×512 cells mesh whereas our simulation is run on a 200×375 cells mesh for the same CPU reason.

This comparison is shown in Figure 13.

The results from our model are in global agreement with the incompressible model results. The overturning and the formation of the air pocket in the curl are accurate. The diffusion is observed to be stronger in our model. This is probably due to the use of a coarser mesh.

The splash up in our simulation has a weaker energy compared with the incompressible case. This may be due to the coarser mesh that, by strongly diffusing this thin jet, reduces the mass in the jet, and thus its momentum. Another explanation is that the limit of the incompressibility criterion, mentioned earlier, used in our model is reached. In this way, a light compressibility would be responsible for smoothing the dynamics of the jet rebound, which shows less elasticity.

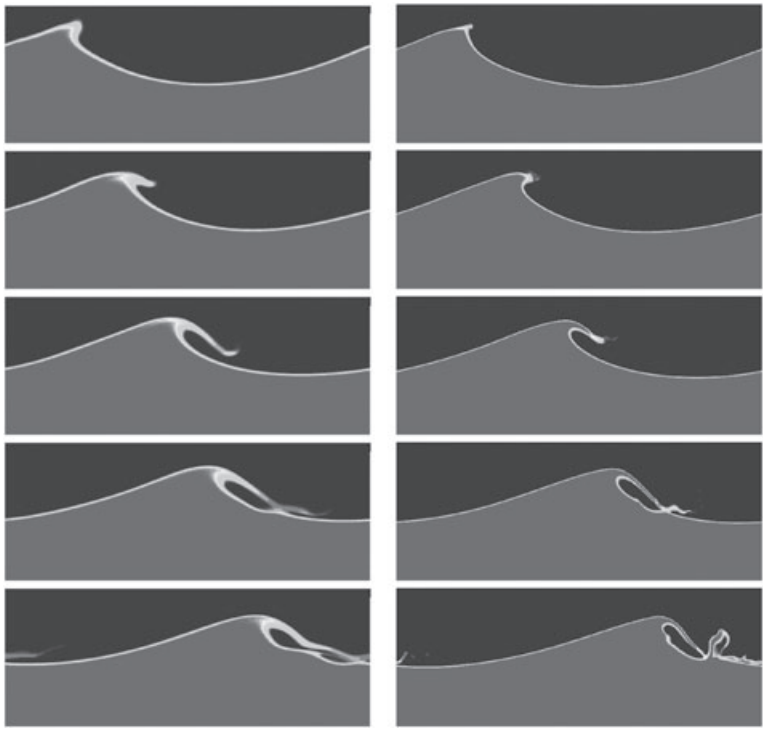

Figure 13. Free-surface dynamics, comparison between our model (left) and Duval's model [18](right) for the breaking of Stokes wave ($Re = 10^4$, steepness $= 0.45$) for non-dimensional times: $\frac{t}{T} = \{0.5719, 0.7019, 0.8319, 0.9619, 1.0919\}$.

5. CONCLUSION

In this paper, a numerical model designed for the modelling of water-wave impacts on a structure has been presented. It includes the effects of entrapped air pockets as well as those of wave-breaking-generated air bubbles in the water. A compressible multifluid method that relies on a three-fluid approach has been developed. The first fluid represents the continuous air fraction and the second and third fluids represent the mixture of the continuous water fraction and the dispersed air fraction (air bubbles). Each fluid is governed by a particular equation of state related its own properties. Compressible Navier–Stokes equations are solved for the equivalent fluid. This model proved to lead to an accurate sound speed in the mixture.

The numerical method is based on a second-order Runge–Kutta scheme in time. At each stage a fractional-step method involving a transport step and a relaxation step is used. In the transport step, the conservation equations are solved assuming frozen pressures and using a Godunov scheme for the flux function on the basis of linear approximations of the equations of state, and for which the second order in space is obtained thanks to the MUSCL method. In the relaxation step, the pressures are released to restore pressure equilibrium.

The accuracy of the model in representing the acoustic properties of a bubbly liquid has been proved using comparison with bubbly-column experiments by [14]. A good agreement for sound speed and wave attenuation has been observed except for frequencies close to the bubble resonant frequency, which does not present a significant weakness with respect to wave impact applications. In addition, a good agreement with the theory for the propagation of a shock wave in a gas–liquid mixture is obtained, allowing to model strong impacts where non-linear effects are expected. Finally, we ran a test case to assess the ability of our model to represent a typical complex free-surface dynamics observed in wave impact. The results showed good agreement with an incompressible model.

REFERENCES

1. Oumeraci H, Bruce T, Klammer P, Easson W. PIV-measurements of breaking wave kinematics and impact loading of caisson breakwaters. *4th International Conference on Port Engineering in Developing Countries 3*, 1995; 2394–2410.
2. Schmidt R, Oumeraci H, Partenscky HW. Impact loads induced by plunging breakers on vertical structures. *Proceedings of the 23rd International Conference on Coastal Engineering*, ASCE, Venice, 1992; 1545–1558.
3. Bullock G, Obhrai C, Peregrine D, Bredmose H. Violent breaking wave impacts. Part 1: results from large-scale regular wave tests on vertical and sloping walls. *Coastal Engineering* 2007; **54**:602–617.
4. Kleefsman K, Fekken G, Veldman A, Iwanowski B, Buchner B. A volume-of-fluid based simulation method for wave impact problems. *Journal of Computational Physics* 2005; **206**:363–393.
5. Wemmenhove R. Numerical simulation of hydrodynamic wave loading by a compressible two-phase model. *European Conference on Computational Fluid Dynamics ECCOMAS CFD 2006*, 2006.
6. Peregrine DH. Water-wave impact on walls. *Annual Review of Fluid Mechanics* 2003; **35**:23–43.
7. Chanteperdrix G. Modélisation et simulation numérique d'écoulements diphasiques interface libre. application l'étude des mouvements de liquides dans les réservoirs de véhicules spatiaux. *PhD Thesis*, Ecole Nationale Supérieure de l'Aéronautique et de l'Espace, Toulouse, France (in French), 2004.
8. Saurel R, Abgrall R. A multiphase Godunov method for compressible multifluid and multiphase flows. *Journal of Computationnal Physics* 1999; **150**:425–467.
9. Wood A. *A Textbook of Sound*. G. Bell: London, 1941.
10. Drew DA. Mathematical modeling of two-phase flow. *Annual Review of Fluid Mechanics* 1983; **15**:261–291.
11. Brackbill J, Kothe D, Zemach C. A continuum method for modeling surface tension. *Journal of Computationnal Physics* 1992; **100**:335–354.
12. Saurel R, Abgrall R. A simple method for compressible multifluid flows. *SIAM Journal on Scientific Computing* 1999; **21**(3):1115–1145.
13. Chanteperdrix G, Villedieu P, Vila J. A compressible model for separated two-phase flows computations. *2002 ASME Fluids Engineering Division Summer Meeting*, Montréal, Quebec, Canada, 2002.
14. Silberman E. Sound velocity and attenuation in bubbly mixtures measured in stranding wave tubes. *Journal of the Acoustical Society of America* 1957; **29**(8):925–933.
15. Commander KW, Prosperetti A. Linear pressure waves in bubbly liquids: comparison between theory and experiments. *Journal of the Acoustical Society of America* 1989; **85**(2):732–746.
16. Peregrine DH, Bredmose H, Bullock G, Obhrai C, Muller G, Wolters G. Violent water wave impact on a wall. *Rogue Waves, Proceedings of the Aha Huliko a Hawaiian Winter Workshop*, 2005; 155–159.
17. Saurel R, Le Metayer O, Massoni J, Gavrilyuk S. Shock jump relations for multiphase mixtures with stiff mechanical relaxation. *Shock Waves* 2007; **16**(3):209–232.
18. Duval M. Etude du déferlement d'une onde de Stokes et de la dissipation associée par simulation directe. *PhD Thesis*, Institut National Polytechnique de Toulouse, France (in French), 2007.